Role of the rare earth in lattice and magnetic coupling in multiferroic $h-HoMnO_3$

J. Liu,[1] Y. Gallais,[1] M.-A. Measson,[1] A. Sacuto,[1] S. W. Cheong,[2] and M. Cazayous[1]

[1]*Laboratoire Matériaux et Phénomènes Quantiques UMR 7162 CNRS, Université Paris Diderot-Paris 7, 75205 Paris cedex 13, France*

[2]*Rutgers Center for Emergent Materials and Department of Physics and Astronomy, Rutgers University, 136 Frelinghuysen Road, Piscataway, New Jersey 08854, USA*

(Received 28 February 2017; published 3 May 2017)

We used Raman scattering to study the lattice and magnetic excitations in the hexagonal $HoMnO_3$ single crystals. The E_2 phonon mode at 237 cm^{-1} is affected by the magnetic order. This mode is related to the displacement of Mn and O ions in the a–b plane and modulates the Mn-O-Mn bond angles in the a–b plane and in the in-plane Mn-Mn superexchange interaction. The mode at 269 cm^{-1} associated to the displacement of the apical Ho^{3+} ions along the c direction presents an abrupt change of slope at T_N, showing that the role of the rare-earth ions cannot be neglected in the magnetic transition. We have identified magnon and crystal-field excitations. The temperature dependence of the magnetic excitations has been compared to the Mn and Ho moment and indicates that the exchange-interaction pattern between Mn and Ho atoms drives the uniaxial anisotropy gap above the Mn-spin-rotation transition.

DOI: 10.1103/PhysRevB.95.195104

I. INTRODUCTION

Multiferroics [1], which exhibit coexistence of magnetism and ferroelectricity with cross coupling, are of great scientific and technological interest for further spintronics, magnonics, and nanoelectronic devices. These include new forms of magnetoelectric memories, electrically controlled magnonic elements, or domain-wall-based devices with engineered magnetic structure [2–6]. Additionally, these compounds can combine multiferroic orders and geometrical frustrations at low dimensionality that provide unusual spin dynamics as well as phase transitions [7].

Rare-earth manganites ($RMnO_3$) are one of the canonical examples of multiferroics and are one of the most investigated families. These compounds crystallize in two different structures as a function of the ionic radius: orthorhombic structures for larger ionic radius (R = La, Ce, Pr, Nd, Sm, Eu, Gd, Tb, Dy) and hexagonal structure (space group $P6_3cm$) for R with smaller ionic radius (R = Ho, Er, Tm, Yb, Lu, Y) [8–10]. Both exhibit multiferrocity, but the microscopic origins are different. The magnetic frustrations in the orthorhombic manganites lead to spin-lattice coupling induced by the inverse Dzyaloshinski-Moriya interaction [9]. The ferroelectricity in the hexagonal compounds results from electrostatic and size effects that lead to the bulking of MnO_5 bipyramids and the displacement of the rare-earth ions [11].

For each rare-earth manganite, the interactions between the lattice and magnetic degrees of freedom need to be clarified. Hexagonal $HoMnO_3$ is one of the most studied of the rare-earth manganites and has a magnetic field-temperature phase diagram that exhibits a multitude of complex spin structures [12–14]. Recently, the antiferromagnetic spin dynamics in $HoMnO_3$ has been studied, tracking the changes in the magnon modes with Thz pulses [15]. The development of the time-resolved experiments to probe the phonon and spin dynamics show the importance of first understanding the static interactions. Moreover, the stability of a magnetic configuration rather than another and the nature of the spin waves have to be understood. The magnetic properties of h–$HoMnO_3$ rare-earth manganite have been studied by inelastic neutron scattering [16], second harmonic generation [13,14], and low-heat transport [17], whereas the lattice vibrations have been investigated by Raman and infrared [18] spectroscopy. However, the studies of the static coupling between the lattice and magnetic degrees of freedom on $HoMnO_3$ single crystals remain small in number [19,20].

Here, we have investigated the A_1 and E_2 phonon modes of h–$HoMnO_3$ with polarized Raman spectroscopy. The temperature dependence of particular phonon modes associated to motions modulating the super-superexchange paths between adjacent Mn planes and modulating the Mn-O-Ho interactions shows that the Mn-Mn and Ho-Mn interaction along the c axis plays an important role in the magnetic ordering in h–$HoMnO_3$. The magnetic excitations have also been measured and spin excitations have been identified. The temperature behavior of the magnon modes shows that the interaction between the rare earth and the Mn atoms controls the uniaxial anisotropy gap from T_N down to the Mn-spin-rotation transition.

II. EXPERIMENTAL DETAILS

$HoMnO_3$ single crystals were grown using the high-temperature flux growth technique in a platinum crucible [21]. The crystals are millimeter-size platelets with a thickness around 0.1 mm and a large surface of 0.5 cm^2. The hexagonal c axis is perpendicular to the surface. The crystals have been polished to obtain high surface quality for optical measurements. Raman scattering is performed in backscattering geometry using the 532 nm excitation line from a laser diode and collected by a triple spectrometer Jobin Yvon T64000 equipped with a liquid-nitrogen-cooled charged-coupled device (CCD). The high rejection rate of the spectrometer allows one to detect the low-frequency excitations. Measurements between 10 and 300 K have been performed using an ARS closed-cycle He cryostat.

III. RESULTS AND DISCUSSION

$HoMnO_3$ crystallizes in a hexagonal lattice, space group $P6_3cm$. This compound is formed by layers of corner-sharing trigonal MnO_5 bipyramids arranged in a layered-type structure

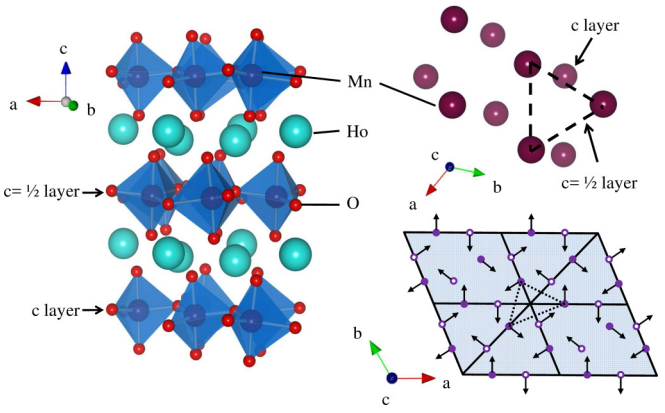

FIG. 1. Crystallographic structure of hexagonal $HoMnO_3$ ($P6_3cm$ phase) and the magnetic order.

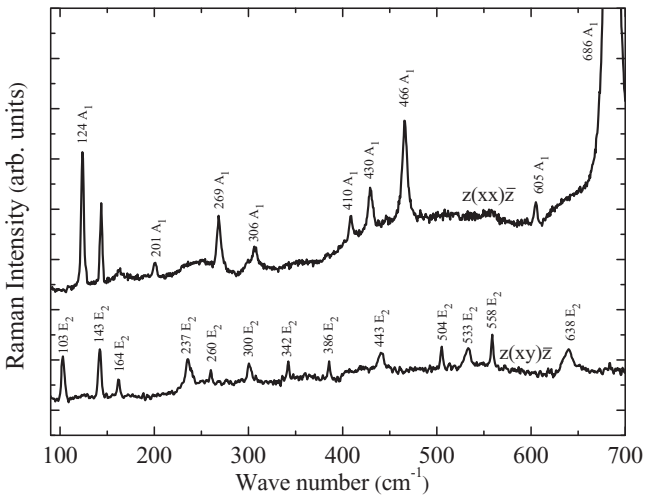

FIG. 2. Phonon modes in h–$HoMnO_3$ single crystal observed at 10 K using $z(xx)=\bar{z}$ (A_1 modes) and $z(xy)=\bar{z}$ (E_2 modes) scattering configurations.

in the a–b plane with apical (O_1, O_2) and in-plane (O_3, O_4) oxygen ions as shown in Fig. 1 [22]. Between the bipyramid layers, the rare-earth ion layers are stacked along the c axis. Ferroelectric polarization appears along the c axis below 875 K and results from electrostatic and size effects that lead to the buckling of MnO_5 bipyramids and the displacement of the Ho^{3+} ions out of the (a,b) plane [11,22]. The moments of Mn^{3+} ions display antiferromagnetic (AF) orderings at $T_{N,Mn}=75$ K. The Mn^{3+} ions form triangular planar sublattices and the AF exchange coupling among Mn^{3+} moments is geometrically frustrated (see Fig. 1). Below $T_{N,Mn}$, the Mn magnetic moments order in 120° arrangements [23]. Another transition occurs below 40 K and implies an in-plane Mn spin reorientation by 90° [12,13,23]. Ho moments of the 4b sites are antiferromagnetically coupled within a given layer and Ho^{3+} ions display AF orderings at $T_{N,Ho}=4.6$ K. It has been proposed that the Ho^{3+} moments are oriented along the c axis with an Ising-type anisotropy. The Ho^{3+} ions present in two different crystallographic sites form two sublattices that can order in parallel or antiparallel orientations [24,25]. The c and $c=+1/2$ layers are ferromagnetically coupled.

A. Lattice excitations

The crystal symmetries define the matrix elements of the Raman tensor which are selected by the incident and scattered light polarizations. Thus selection rules define the vibrational modes that can be detected by Raman spectroscopy. The group-theoretical analysis shows that the zone-center phonon modes (Γ point) are in the irreducible representations of the C_{6v}: $10A_1+5A_2+10B_1+5B_2+15E_1+15E_2$. Only 38 of these modes are Raman active: $\Gamma_{Raman}=9A_1+14E_1+15E_2$. Using different scattering configurations, it is possible to choose the mode to activate [26]. Here we used the incident wave vector antiparallel to the scattered one (backscattering configuration). The longitudinal optical A_1 modes are activated when the phonon propagation direction corresponds to the direction of the ions displacements using the $z(xx)=\bar{z}$ polarization configuration. Pure E_2 modes are obtained using $z(xy)=\bar{z}$ geometry.

Figure 2 presents the Raman spectra measured on h–$HoMnO_3$ single crystals with the $z(xx)=\bar{z}$ and $z(xy)=\bar{z}$ scattering configurations. The Raman selection rules allow us to identify the 9 A_1 modes and 13 E_2 modes over 15. The frequencies of the phonon modes at 10 K are reported in Table I and compared to the previous theoretical results on single crystal [18]. We have measured the temperature dependences of the phonon modes in order to identify the effect of the phase transitions.

TABLE I. A_1 and E_2 mode frequencies (cm^{-1}) measured in h–$HoMnO_3$ and description of the atomic displacements.

Mode	This work	Theory [18]	Direction of the largest displacement
A_1	124	127	z(Ho)
	201	234	Rot x,y(MnO_5)
	269	270	$+z$(Ho)$-z$(Mn)
	306	295	x(Mn), z(O_3)
	410	428	$+z$(O_3,O_4)$+x$, y(O_2)$-x,y$(O_1)
	430	460	$+z$(O_4,O_3),$-z$(Mn)
	466	474	$+x,y$(O_1,O_2), $-x,y$(Mn)
	605	614	$+z$(O_1,O_2)$-z$(Mn)
	686	673	$+z$(O_1)$-z$(O_2)
E_2		64	x,y(Ho,Mn)
	103	96	$+x,y$(Mn,O_3,O_4)$-x,y$(Ho)
	143	137	x,y(Ho)
	164	152	x,y(Ho)
	237	231	$+x,y$(Mn),$-x,y$(O_3,O_4)
		254	z(Mn,O_2,O_1)
	260	265	z(Mn,O_1,O_2)
	300	330	z(O_2,O_1), x,y(O_4)
	342	339	$+x,y$(O_1,O_2,O_3,O_4)$-x,y$(Mn)
	386	402	$+x,y$(O_1,O_4)$-x,y$(O_2,Mn)
	443	468	$+x,y$(O_4)$-x,y$(O_1,Mn)
	504	523	x,y(O_4,O_3,O_1,O_2)
	533	557	x,y(O_4)
	558	583	x,y(O_4,O_3)
	638	649	x,y(O_3,O_4)

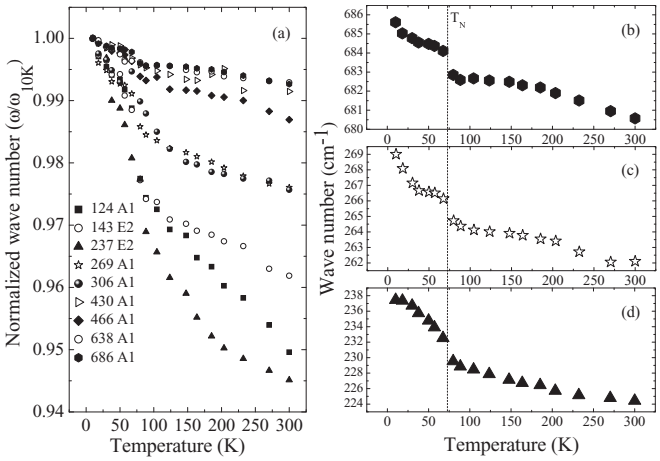

FIG. 3. (a) Normalized wave numbers $[\omega(T)/\omega(10\,K)]$ of 7 A_1 and 2 E_2 modes and wave numbers of the (b) A_1 mode at 686 cm^{-1}, (c) A_1 mode at 269 cm^{-1}, and (d) E_2 mode at 237 cm^{-1} as a function of temperature.

Figure 3(a) presents the normalized frequencies over the frequency at 10 K of several A_1 and E_2 modes as a function of temperature. All the phonon frequencies soften due to the dilation of the unit cell when temperature increases. Three phonon modes present an abrupt change in their frequencies, as shown in Figs. 3(b)–3(d) as the fingerprint of the spin-phonon coupling in the magnetically ordered phase.

The E_2 mode at 237 cm^{-1} presents a frequency shift beyond the mean behavior of the other modes [Fig. 3(a)] and an abrupt change of slope around the Néel temperature in Fig. 3(d). This phonon mode is related to the displacement of Mn and O ions in the a–b plane and it modulates the in-plane Mn-Mn superexchange interaction and the Mn-O-Mn bond angles in the a–b plane. Such a behavior has already been measured in rare-earth manganites, such as in $YbMnO_3$ single crystals [27]. The peaks at 269 and 686 cm^{-1} show the same behavior at the Néel temperature.

The mode at 269 cm^{-1} is associated to the relative displacement of the apical Ho^{3+} ions along the c direction. The role played by the R element in the $RMnO_3$ manganites has been underestimated. However, the role of the nonmagnetic R atom is not negligible as underlined by the temperature behavior of the Ho^{3+} ions frequency at the the Néel temperature.

The mode at 686 cm^{-1} is related to the relative displacement of the apical oxygen ions along the c direction and modulates the Mn-O-O-Mn bond angles. Notice that the interplanar coupling between Mn cations and two O anions (Mn-O-O-M) corresponds to the interplanar super-superexchange paths. The abrupt change of slope at T_N shows that the super-superexchange path through the apical oxygen participates in the three-dimensional magnetic ordering.

B. Spin excitations

Figure 4(b) shows the low-frequency Raman spectra measured on a h–$HoMnO_3$ single crystal at 10 K. Three peaks are measured: $P_1 = 13$ cm^{-1}, $P_3 = 25$ cm^{-1}, $P_2 = 41$ cm^{-1} with two polarization configurations. Remember that Raman scattering can probe, in addition to phonon modes, the crystal

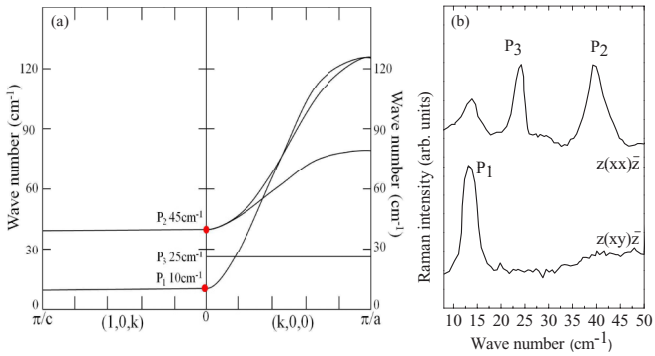

FIG. 4. (a) Magnon dispersions along $\mathbf{k}=(1,0,k)$ and $\mathbf{k}=(k,0,0)$ extracted from Ref. [16]. (b) Raman spectra of low-frequency excitations measured at 10 K in $z(xx)\bar{z}$ and $z(xy)\bar{z}$ configuration.

field, one magnon (zone-center) excitations, and two-magnon (zone-edge) excitations. Below 50 cm^{-1}, there are no phonon modes and, as shown in the following paragraph, the P_1, P_2, and P_3 peaks disappear at the Néel temperature, so these peaks can be thus attributed to magnetic excitations. In order to determine the origin of the magnetic excitations, we have compared our measurements to neutron-scattering results. Figure 4(a) represents the magnetic excitation dispersions along the $\mathbf{k}=(1,0,k)$ and $\mathbf{k}=(k,0,0)$ axes [16]. At the Γ point, the mode at 10 cm^{-1} corresponds to the uniaxial anisotropy gap and can be associated to the P_1 peak. The mode at 45 cm^{-1} in Fig. 4(a) is split at higher energies at the zone edge with a higher branch around 130 cm^{-1} and a lower branch around 80 cm^{-1}. The P_2 peak can be attributed to this mode and corresponds to the one-magnon mode of the Mn^{3+} magnetic structure in the (a,b) plane, in particular to the global in-phase and out-of-phase rotations of the 120° pattern inside the basal plane. The P_3 is related to the crystal-field excitation at 25 cm^{-1}, which presents a flat dispersion as shown by neutron scattering [16]. Transition from the ground state of

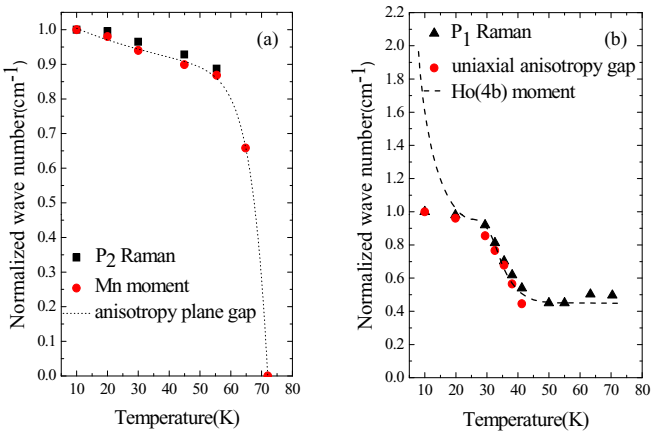

FIG. 5. Temperature dependence of normalized wave number $[\omega(T)/\omega(10\,K)]$ of (a) the magnetic mode P_2 compared with the Mn moments and the energy of the anisotropy plane gap [28], and of (b) the P_1 mode compared to the uniaxial energy gap and the Ho(4b) moment [28].

the $4f$ ions to the excited state are, in principle, Raman active and correspond to crystal-field excitations.

The temperature dependence of the magnon wave number P_1 and P_2 recorded from 10 to 70 K is shown in Fig. 5.

In Fig. 5(a), the Raman shift of the P_2 mode decreases as the temperature is increased. This conventional softening is first compared to the one of the Mn moment. The good agreement with the variation of the Mn moment shows that this magnon mode can be thus associated to the spin excitations of the Mn^{3+} ions. It also agrees well with the temperature dependence of the anisotropy plane gap measured by neutron scattering [28]. The P_2 peak is the signature of the anisotropy planar gap in the (a,b) plane and varies with temperature similar to the Mn^{3+} ion moment.

In Fig. 5(b), the P_1 peak wave number presents a change in the slope between 30 and 40 K. We have compared this behavior to the thermal evolution of the uniaxial gap [28]. The good agreement confirms that this peak is related to the uniaxial anisotropy gap. At $T_{SR} = 33$ K, a Mn-spin-rotation transition has been observed, implying an in-plane Mn-spin reorientation by 90° and an antiferromagnetic order of the Ho moments along the c axis. To shed some light on the role of the Ho ions, we have drawn in Fig. 5(b) the temperature dependence of Ho moments. The P_1 peak frequency shift is close to the behavior of the Ho moment down to T_{SR}. This evidence points out the role of the Ho^{3+} ion moment and of the Ho-Mn interaction on the P_1 spin wave. Below T_{SR}, the uniaxial gap is no longer correlated to the Ho moment. Those measurements show that the exchange-interaction pattern between the rare earth and Mn atoms is a key to understand the uniaxial anisotropy gap but not sufficient below the Mn-spin-rotation transition.

IV. CONCLUSION

In summary, our measurements show that the E_2 mode associated to the relative displacement of the apical Ho^{3+} ions along the c direction is sensitive to the the Néel temperature, pointing out the non-negligible role played by the R element in the $RMnO_3$ manganites. We also reveal the spin excitations and the role played by the Ho^{3+} ion moment and of the Ho-Mn interaction on the uniaxial anisotropy gap.

[1] W. Eerenstein, N. D. Mathur, and J. F. Scott, Nature (London) **442**, 759 (2006).

[2] J. Allibe, S. Fusil, K. Bouzehouane, C. Daumont, D. Sando, E. Jacquet, C. Deranlot, M. Bibes, and A. Barthélémy, Nano Lett. **12**, 1141 (2012).

[3] P. Rovillain, R. De Sousa, Y. Gallais, A. Sacuto, M. Méasson, D. Colson, A. Forget, M. Bibes, A. Barthélémy, and M. Cazayous, Nat. Mater. **9**, 975 (2010).

[4] Y. Kajiwara, K. Harii, S. Takahashi, J. Ohe1, K. Uchida, M. Mizuguchi, H. Umezawa, H. Kawai, K. Ando, K. Takanashi, S. Maekawa, and E. Saitoh, Nature (London) **464**, 262 (2010).

[5] S. O. Demokritov and A. N. Slavin, *Magnonics: From Fundamentals to Applications* (Springer-Verlag, Berlin, 2013).

[6] J. H. Lee, I. Fina, X. Marti, Y. H. Kim, D. Hesse, and M. Alexe, Adv. Mater. **26**, 7078 (2014).

[7] T. Kimura, T. Goto, H. Shintani, K. Ishizaka, T. Arima, and Y. Tokura, Nature (London) **426**, 55 (2003).

[8] M. Fiebig, J. Phys. D **38**, R123 (2005).

[9] S. W. Cheong and M. Mostovoy, Nat. Mater. **6**, 13 (2007).

[10] J. Park, J. G. Park, G. S. Jeon, H. Y. Choi, C. H. Lee, W. Jo, R. Bewley, K. A. McEwen, and T. G. Perring, Phys. Rev. B **68**, 104426 (2003).

[11] B. B. Van Aken, T. T. M. Palstra, A. Filippetti, and N. A. Spaldin, Nat. Mater. **3**, 164 (2004).

[12] A. Muñoz, J. A. Alonso, M. J. Martinez-Lope, M. T. Casais, J. L. Martinez, and M. T. Fernandez-Diaz, Chem. Mater. **13**, 1497 (2001).

[13] M. Fiebig, D. Fröhlich, K. Kohn, S. Leute, Th. Lottermoser, V. V. Pavlov, and R. V. Pisarev, Phys. Rev. Lett. **84**, 5620 (2000).

[14] M. Fiebig, C. Degenhardt, and R. V. Pisarev, J. Appl. Phys. **91**, 8867 (2002).

[15] P. Bowlan, S. A. Trugman, J. Bowlan, J. X. Zhu, N. J. Hur, A. J. Taylor, D. A. Yarotski, and R. P. Prasankumar, Phys. Rev. B **94**, 100404 (2016).

[16] X. Fabrèges, S. Petit, I. Mirebeau, S. Pailhes, L. Pinsard, A. Forget, M. T. Fernandez-Diaz, and F. Porcher, Phys. Rev. Lett. **103**, 067204 (2009).

[17] X. M. Wang, C. Fan, Z. Y. Zhao, W. Tao, X. G. Liu, W. P. Ke, X. Zhao, and X. F. Sun, Phys. Rev. B **82**, 094405 (2010).

[18] A. P. Litvinchuk, M. N. Iliev, V. N. Popov, and M. M. Gospodinov, J. Phys.: Condens. Matter **16**, 809 (2004).

[19] C. dela Cruz, F. Yen, B. Lorenz, Y. Q. Wang, Y. Y. Sun, M. M. M. Gospodinov, and C. W. Chu, Phys. Rev. B **71**, 060407(R) (2005).

[20] M. Poirier, J. C. Lemyre, P. O. Lahaie, L. Pinsard-Gaudart, and A. Revcolevschi, Phys. Rev. B **83**, 054418 (2011).

[21] T. Choi, Y. Horibe, H. T. Yi, Y. J. Choi, W. Wu and S.-W. Cheong, Nat. Mater. **9**, 423 (2010).

[22] T. Lottermoser, T. Lonkai, U. Amann, D. Hohlwein, J. Ihringer, and M. Fiebig, Nature (London) **430**, 541 (2004).

[23] O. P. Vajk, M. Kenzelmann, J. W. Lynn, S. B. Kim, and S.-W. Cheong, Phys. Rev. Lett. **94**, 087601 (2005).

[24] P. J. Brown and T. Chatterji, Phys. Rev. B **77**, 104407 (2008).

[25] N. Hur, I. K. Jeong, M. F. Hundley, S. B. Kim, and S. W. Cheong, Phys. Rev. B **79**, 134120 (2009).

[26] S. P. S. Porto, J. A. Giordmaine, and T. C. Damen, Phys. Rev. **147**, 608 (1966).

[27] J. Liu, C. Toulouse, P. Rovillain, M. Cazayous, Y. Gallais, M.-A. Measson, N. Lee, S. W. Cheong, and A. Sacuto, Phys. Rev. B **86**, 184410 (2012).

[28] X. Fabrèges, Ph.D. thesis, University Paris-Sud 11, France, 2010.